

The different baryonic Tully-Fisher relations at low masses.

Chris B. Brook^{1,2*}, Isabel Santos-Santos¹, Greg Stinson³

¹*Departamento de Física Teórica, Universidad Autónoma de Madrid, 28049 Cantoblanco, Madrid, Spain*

²*Astro-UAM, UAM, Unidad Asociada CSIC*

³*Max-Planck-Institut für Astronomie, Königstuhl 17, 69117 Heidelberg, Germany*

Accepted XXXX . Received XXXX; in original form XXXX

ABSTRACT

We compare the Baryonic Tully-Fisher relation (BTFR) of simulations and observations of galaxies ranging from dwarfs to spirals, using various measures of rotational velocity V_{rot} . We explore the BTFR when measuring V_{rot} at the flat part of the rotation curve, V_{flat} , at the extent of HI gas, V_{last} , and using 20% (W_{20}) and 50% (W_{50}) of the width of HI line profiles. We also compare with the maximum circular velocity of the parent halo, $V_{\text{max}}^{\text{DM}}$, within dark matter only simulations. The different BTFRs increasingly diverge as galaxy mass decreases. Using V_{last} one obtains a power law over four orders of magnitude in baryonic mass, with slope similar to the observed BTFR. Measuring V_{flat} gives similar results as V_{last} when galaxies with rising rotation curves are excluded. However, higher rotation velocities would be found for low mass galaxies if the cold gas extended far enough for V_{rot} to reach a maximum. W_{20} gives a similar slope as V_{last} but with slightly lower values of V_{rot} for low mass galaxies, although this may depend on the extent of the gas in your galaxy sample. W_{50} bends away from these other relations toward low velocities at low masses. By contrast, $V_{\text{max}}^{\text{DM}}$ bends toward high velocities for low mass galaxies, as cold gas does not extend out to the radius at which halos reach $V_{\text{max}}^{\text{DM}}$. Our study highlights the need for careful comparisons between observations and models: one needs to be consistent about the particular method of measuring V_{rot} , and precise about the radius at which velocities are measured.

Key words: galaxies: evolution - formation - haloes cosmology: theory - dark matter

1 INTRODUCTION

Galaxies follow a tight relation between optical luminosity and the width of the 21 cm line of neutral hydrogen HI (Tully & Fisher 1977). The 21 cm line-width is a measure of rotation velocity V_{rot} which reflects total mass within a given radius, while luminosity is a reflection of stellar mass. Other measures of V_{rot} have subsequently been used in deriving the Tully-Fisher relation, using information from the full rotation curves of galaxies (e.g. Verheijen 2001; McGaugh 2005; Kuzio de Naray et al. 2006; Noordermeer & Verheijen 2007; Yegorova & Salucci 2007; Oh et al. 2011), and luminosity is often converted to stellar masses, making the relation between V_{rot} and stellar mass more explicit.

For low mass galaxies, which become increasingly gas rich (Geha et al. 2006; Bradford et al. 2015), a tighter relation is found when V_{rot} is plotted against the total observable baryonic mass M_b , i.e. stellar mass plus cold gas mass (Freeman 1999; McGaugh et al.

2000). As argued in McGaugh (2012), the gas dominance in low mass galaxies minimises the importance of the error in stellar mass, allowing relatively accurate measurements of M_b when deriving the baryonic Tully-Fisher relation (BTFR).

However, low mass galaxies are more problematic when it comes to determining V_{rot} . For high mass galaxies, rotation curves generally rise sharply (Roberts & Rots 1973; Rubin et al. 1978), and some then drop before flattening at the outer parts (e.g. Sofue & Rubin 2001; Noordermeer & Verheijen 2007), at a velocity which can then be defined as V_{flat} , a common measure of V_{rot} used in BTFRs. By contrast, rotation curves of low mass galaxies rise more gently (e.g. Lelli et al. 2013) and although they do start to flatten beyond about 2 disc scale-lengths, they are often still rising at the last measured point (e.g. Catinella et al. 2006; Swaters et al. 2009). To extend the V_{flat} BTFR to low mass galaxies, Stark et al. (2009) select galaxies with rotation curves that are approximately flat in their outer regions, according to some flatness criteria.

The low mass end of the BTFR is also problematic when measuring V_{rot} using HI line widths. The discrepancy between measuring the HI line-width at 20 per cent (W_{20}) and 50 per cent (W_{50}) of its peak value is typically 25 km s^{-1} (Koribalski et al. 2004; Brad-

* E-mail: cbabrook@gmail.com

Table 1. Properties of the MaGICC galaxies ordered by halo mass. R_{HI} and V_{last} are measured at $\dagger N_{\text{HI}}=1\text{M}_{\odot}/\text{pc}^2$ and $\P N_{\text{HI}}=10^{19}\text{cm}^{-2}$

Name	M_{halo} (M_{\odot})	M_{*} (M_{\odot})	M_{HI} (M_{\odot})	h_I (kpc)	R_{HI}^{\dagger} (kpc)	R_{HI}^{\P} (kpc)	$V_{\text{last}}^{\dagger}$ (km/s)	V_{last}^{\P} (km/s)	R_{flat} (kpc)	V_{flat} (km/s)	W_{20} (km/s)	W_{50} (km/s)	$R_{\text{max}}^{\text{DM}}$ (kpc)	$V_{\text{max}}^{\text{DM}}$ (km/s)
g15784_MW	1.49×10^{12}	5.67×10^{10}	4.04×10^{10}	3.23	31.9	46.3	225.7	212.0	26.8	218.8	500.5	404.8	54.90	183.0
g21647_MW	8.24×10^{11}	2.51×10^{10}	8.51×10^9	1.30	14.5	33.9	164.4	150.7	17.1	157.5	390.0	350.0	38.15	161.6
g1536_MW	7.10×10^{11}	2.36×10^{10}	1.20×10^{10}	3.46	33.2	42.0	165.8	157.6	8.48	170.8	386.2	349.9	52.86	142.9
g5664_MW	5.39×10^{11}	2.74×10^{10}	7.25×10^9	2.34	17.4	42.4	162.4	137.6	12.6	169.0	399.8	368.5	39.15	124.6
g7124_MW	4.47×10^{11}	6.30×10^9	6.99×10^9	2.79	15.3	30.7	126.0	120.7	12.3	118.2	218.6	154.8	38.15	135.1
g15807_Irr	2.82×10^{11}	1.46×10^{10}	7.66×10^9	1.94	17.0	25.9	134.7	123.3	10.4	137.0	289.4	179.2	32.99	101.0
g15784_Irr	1.70×10^{11}	4.26×10^9	5.11×10^9	2.27	12.8	19.6	110.4	104.1	12.2	104.8	210.4	183.6	27.45	91.51
g22437_Irr	1.10×10^{11}	7.44×10^8	1.87×10^9	1.88	7.87	12.4	75.95	77.14	6.44	69.44	141.0	104.9	27.32	66.69
g21647_Irr	9.65×10^{10}	1.98×10^8	9.55×10^8	1.75	7.74	21.2	60.51	61.89	7.70	56.15	111.1	80.00	19.08	80.81
g1536_Irr	8.04×10^{10}	4.46×10^8	1.25×10^9	1.70	7.73	14.9	64.97	68.63	9.14	61.66	94.15	65.37	26.43	71.49
g5664_Irr	5.87×10^{10}	2.36×10^8	7.50×10^8	1.66	6.82	13.6	54.85	61.14	8.92	55.27	105.3	58.36	19.58	62.31
g7124_Irr	5.23×10^{10}	1.32×10^8	7.13×10^8	1.16	7.19	11.1	51.53	54.19	7.37	48.05	81.40	52.73	19.08	67.56
g15807_dIrr	3.04×10^{10}	1.60×10^7	1.31×10^8	1.26	2.96	7.77	29.93	41.86	8.00	41.22	53.70	37.36	16.50	50.49
g15784_dIrr	1.77×10^{10}	8.98×10^6	2.12×10^7	0.73	1.48	2.06	23.26	27.41	3.92	34.09	38.08	18.68	13.73	45.75
g22437_dIrr	1.19×10^{10}	5.05×10^5	1.61×10^7	0.17	1.23	1.59	21.92	23.52	1.08	20.09	27.75	12.79	13.66	36.17
g1536_dIrr	9.69×10^9	7.20×10^5	1.79×10^7	0.17	1.04	1.58	21.72	25.33	1.58	24.10	41.96	16.81	13.22	35.74

ford et al. 2015), which becomes an increasing fraction of the measured rotation velocity at lower masses.

Observational studies have shown that the way V_{rot} is measured (V_{flat} , V_{last} , W_{20} , W_{50}) will result in different T-F and BTF relations (e.g. Verheijen 2001; Noordermeer & Verheijen 2007; McGaugh 2012; Bradford et al. 2016). Further, sample selection also plays a role (Sorce & Guo 2016). Understanding the difference in measured values of V_{rot} has important implications for interpreting the BTFR, which is used as a crucial constraint on theoretical models (e.g. Dutton & van den Bosch 2009; Trujillo-Gomez et al. 2011; McGaugh 2012; Dutton 2012; Brook et al. 2012). As recently shown (Brook & Di Cintio 2015; Brook & Shankar 2015), these differences in measures of V_{rot} also significantly affect the interpretation of the observed velocity function, i.e. the number of galaxies at given V_{rot} within a given volume (Zavala et al. 2009; Obreschkow et al. 2009; Papastergis et al. 2011; Klypin et al. 2014).

In this paper, we explore the BTFR of the MaGICC suite of simulated galaxies (Brook et al. 2012; Stinson et al. 2013), comparing the derived BTFRs when measuring V_{rot} in different ways. We show, in particular, that the different forms of the BTFR become increasingly divergent at low masses. The paper is organized as follows: Sec 2 presents the simulations, describing initial conditions and baryonic modelling. The rotation curves and HI line-widths are shown in Sec 3.1 & 3.2, respectively. The various derived measures of V_{rot} are then shown in Sec 3.3, and the different forms of the BTFR in Sec 3.4, with implications discussed in Sec 4.

2 THE SIMULATIONS

We use ‘zoom’ hydro-dynamical simulations from the MaGICC (Making Galaxies in a Cosmological Context) project (Brook et al. 2012; Stinson et al. 2013). The initial power spectrum is derived from the McMaster Unbiased Galaxy Simulations (Stinson et al. 2010) which use a Λ CDM cosmology with WMAP3 parameters. The simulated galaxies cover a range of merger histories and formation times, but are all isolated. Therefore, whether environment has an effect on our results cannot be answered in this study.

The simulated galaxies are evolved using the parallel N-

body+SPH tree-code GASOLINE (Wadsley et al. 2004), which includes gas hydrodynamics and cooling, star formation, energy feedback and metal enrichment. We describe here the most important implementations (for details see Stinson et al. 2013).

When gas gets cold and dense, stars form at rate $\propto \rho^{1.5}$. Stars feed energy and metals to the surrounding interstellar medium. Energy feedback by supernovae is implemented using the blastwave formalism (Stinson et al. 2006), releasing $\epsilon_{\text{SN}} \times 10^{51}$ erg of thermal energy, where we set $\epsilon_{\text{SN}}=1$, i.e. we release all available SN energy in thermal form, even though observations indicate that a significant amount of the energy is radiated away. The reason is because thermal energy is radiated away rapidly in the simulations for numerical reasons, due to lack of resolution (see Stinson et al. 2013 for a full discussion). The metals deposited from SNe are computed from a Chabrier IMF. The composition of each gas particle is traced throughout the simulation, being comprised of H, He and a range of metals recycled from supernova explosions and deposited to the surrounding gas particles (see Stinson et al. 2006), with metal diffusion between gas particles also included (Shen et al. 2010). GASOLINE includes the effect of a uniform background radiation field on the ionization and excitation state of the gas. Metal-line cooling (Shen et al. 2010) and feedback from massive stars (Stinson et al. 2013) prior to their explosion as SNe are also included.

Radiative cooling has three parts $\Lambda = \Lambda_{\text{H,He}} + \Lambda_{\text{metal}} + \Lambda_{\text{Comp}}$, where $\Lambda_{\text{H,He}}$ is net cooling due to (H, H^+ , He, He^+ and He^{++}), Λ_{metal} is the rate due to metals, and Λ_{Comp} is the Compton cooling and heating. For $\Lambda_{\text{H,He}}$, cooling and heating rates are calculated directly from the ionization equations, meaning the simulations capture the non-equilibrium cooling of primordial species. Each timestep takes the abundance of ions at the end of the previous step as the starting point. Ionization, cooling and heating rates match those of Abel et al. (1997). For calculating HI fractions at $z=0$, we post process to include self-shielding, following Appendix 2 in Rahmati et al. (2013a) and ionization from star forming regions following Rahmati et al. (2013b), using their Eqn 5 which relates star formation to gas surface density. The amount of HI is somewhat sensitive to the manner in which ionization rates are modeled, with neutral hydrogen masses around a factor of two larger using these models than when assuming that the ISM is optically thin.

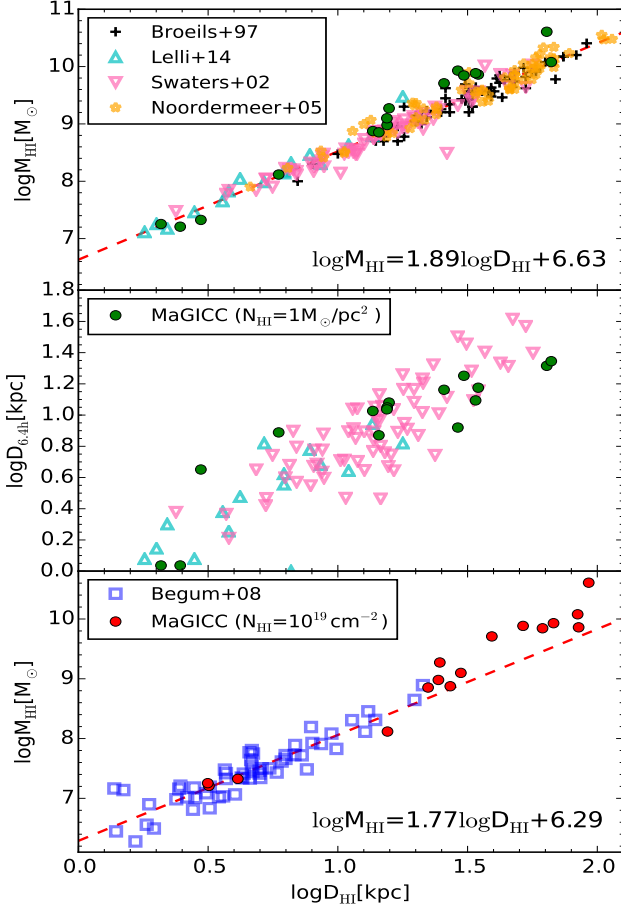


Figure 1. Comparisons of the sizes of the simulated galaxies with observations, in HI gas and star light. Observational data sets are shown in the legends. Top Panel: Green circles show M_{HI} of the simulations as a function of the diameter (D_{HI}) where the HI surface density drops below $1 \text{ M}_{\odot} \text{ pc}^{-2}$. Middle panel: $D_{6.4h}$ as a function of D_{HI} where $D_{6.4h}$ is 6.4 times the disc scale length. Bottom panel: Red circles show D_{HI} where the HI surface density drops below 10^{19} cm^{-2} versus M_{HI} .

There are 16 galaxies, separated into three sub-sets, labelled as Milky-Way (MW), irregular (Irr) and dwarf irregular (dIrr) types, with stellar masses ranging $5 \times 10^5 - 5 \times 10^{10} \text{ M}_{\odot}$. Resolution varies depending on the “type”: MW types have $m_{\text{star}} = 4.0 \times 10^4 \text{ M}_{\odot}$, $m_{\text{gas}} = 5.7 \times 10^4 \text{ M}_{\odot}$, $m_{\text{dm}} = 1.1 \times 10^6 \text{ M}_{\odot}$ and a gravitational softening length of $\epsilon = 312 \text{ pc}$ (for all particle types); Irr’s have $m_{\text{star}} = 4.3 \times 10^3 \text{ M}_{\odot}$, $m_{\text{gas}} = 7.1 \times 10^3 \text{ M}_{\odot}$, $m_{\text{dm}} = 1.4 \times 10^5 \text{ M}_{\odot}$ and $\epsilon = 156 \text{ pc}$; and dIrr’s have $m_{\text{star}} = 5.7 \times 10^2 \text{ M}_{\odot}$, $m_{\text{gas}} = 1.1 \times 10^3 \text{ M}_{\odot}$, $m_{\text{dm}} = 1.7 \times 10^4 \text{ M}_{\odot}$ and $\epsilon = 78 \text{ pc}$.

The halos are identified using AHF (Knollmann & Knebe 2009) with halo masses defined within a sphere containing $\Delta_{\text{vir}} \simeq 350$ times the cosmic matter density at $z=0$. The bulk of the analysis is done using `pynbody` (Pontzen et al. 2013).

For the simulations, we use baryon mass $M_b = M_{\star} + 4/3 \times M_{\text{HI}}$ with the factor of $4/3$ used to account for forms of gas other than HI, in a manner that mimics observational assumptions of the comparison data (e.g. McGaugh 2012). M_{HI} remains an approximation since an accurate model of HI mass would require full radiative transfer. In particular self shielding from the UV background is not included. This uncertainty in the fraction of gas classified as HI will not affect our rotation curve shapes, but may affect the extent of the

HI discs and hence the radius at which we measure V_{rot} . Disk scale lengths are derived from exponential fits to the surface brightness profiles in the I band: each stellar particle from the simulation represents a single stellar population (SSP) for which an absolute magnitude in a particular bandpass is calculated, interpolating between a grid of SSP luminosities from Girardi et al. (2010) and Marigo et al. (2008) for various stellar ages and metallicities. We note that scale-lengths in Swaters et al. 2009 and Lelli et al. 2014 use the R band, which won’t significantly effect the comparison.

Basic galaxy parameters are shown in Table 1, including halo mass (M_{halo}), stellar mass (M_{\star}), HI gas mass (M_{HI}), disc scale length h , the extent of the HI disc R_{HI} , defined as the radius at which the HI density of the galaxy falls to $1 \text{ M}_{\odot} \text{ pc}^{-2}$, which is adopted in several observational studies (eg. Broeils & Rhee 1997; Swaters et al. 2002; Noordermeer et al. 2005; Lelli et al. 2014), although we note that the Begum et al. (2008) data set which comprises a significant fraction of the observed low mass galaxies, uses a threshold of 10^{19} cm^{-2} . We examine both thresholds in Fig 1 which compares the sizes of the simulated galaxies with observations, in HI gas and star light. Observational data come from Broeils & Rhee (1997); Swaters et al. (2002); Noordermeer et al. (2005); Lelli et al. (2014) and Begum et al. (2008).

Fig 1 plots D_{HI} against M_{HI} and $D_{6.4h}$. Green and red circles in the top and bottom panels show the simulations when defining the diameter (D_{HI}) as where the HI surface density drops below $1 \text{ M}_{\odot} \text{ pc}^{-2}$ and 10^{19} cm^{-2} respectively. Fits to the observed $D_{\text{HI}} - M_{\text{HI}}$ relation are shown as red lines. We will use this relation to define a radius $R_{\text{HI}} = D_{\text{HI}}/2$ where we measure the circular velocity V_{last} , which results in a measure of V_{rot} for each simulation at a radius that is similar to that of observed galaxies of the same M_{HI} . $D_{6.4h}$ is defined as 6.4 times the disc scale length, and is used as an indication of the extent of star light in galaxies. This is considered better than using an isophotal diameter at e.g. $25 \text{ B-mag arcsec}^{-2}$, as only a small fraction of the disk is enclosed within the isophotal diameter in low surface brightness galaxies (Swaters et al. 2002).

The simulations fall reasonably within the range of observed galaxies, giving some confidence in the mass distributions of the baryons (see also Santos-Santos et al. 2016). Larger, uniform samples of simulations and observations are required to make careful statistical comparisons including determination of scatter. Regardless, the focus of this paper is on how different measures of V_{rot} give different BTFRs, with which we will proceed.

3 ANALYSIS AND RESULTS

3.1 Rotation curves

Figure 2 shows the circular velocity rotation curves of the simulated galaxies, computed using the gravitational potential of the simulation along the mid-plane of the aligned disc. This is more accurate than just assuming a spherically symmetric potential and averaging mass inside spherical shells (i.e. the classical $V^2 = GM/r$). The contribution from each mass component is plotted as a different linestyle: cold gas thick solid; stars dashed; DM dot-dashed; total, thin solid with circles marking integer multiples of h . Rotation curves are plotted out to R_{HI} , or to R_{flat} , whichever is larger. Vertical dotted (dashed) lines show R_{HI} in cases where $R_{\text{flat}} > R_{\text{HI}}$, using density threshold of $1 \text{ M}_{\odot} \text{ pc}^{-2}$ (10^{19} cm^{-2}).

Whether the shapes of the rotation curves match, in detail, the distribution of observed galaxy rotation curve shapes requires a larger sample of simulations and is beyond the scope of this paper.

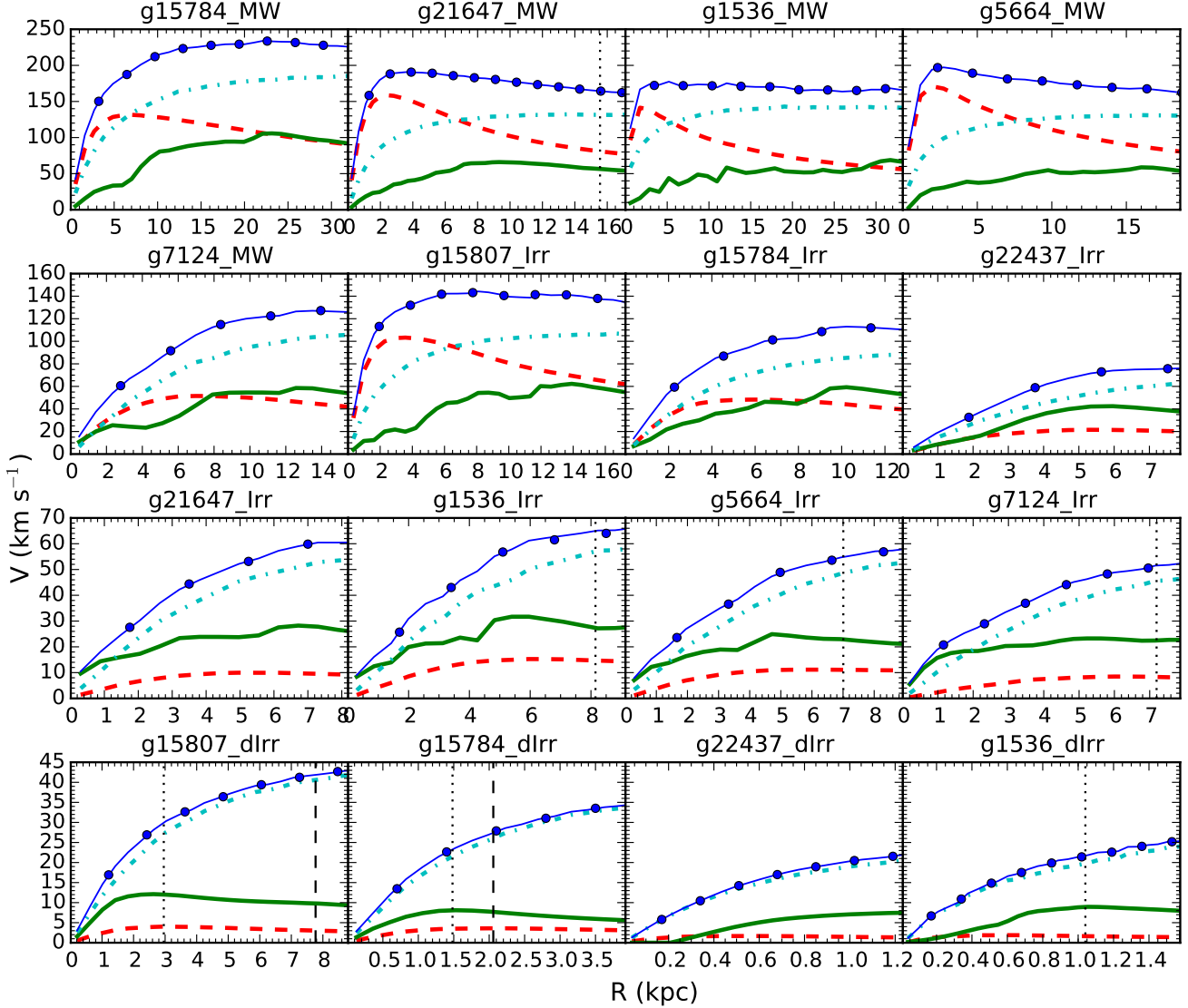


Figure 2. Circular velocity rotation curves of the simulated galaxies, with different lines for the different components: solid for cold gas; dashed for stars; dot-dashed for dark matter; thin solid with circles for total. The circles in the total rotation curve mark multiples of h . The curves extend to R_{HI} , or to R_{flat} in cases of rising rotation curves, in which cases R_{HI} is marked as a dotted (dashed) vertical line when defined at $1 \text{ M}_{\odot} \text{ pc}^{-2}$ (10^{19} cm^{-2}).

We note that Oman et al. (2015) found that the EAGLE simulations (Schaye et al. 2015) were not able to reproduce the variation in rotation curve shapes that is observed, in particular they could not simulate galaxies with slowly rising rotation curves. They showed that the MaGICC simulations, as used here, did form galaxies with such slowly rising rotation curves, as can be seen in Fig 2. Yet some observed low mass galaxies have more steeply rising rotation curves (e.g. Swaters et al. 2009). A larger suite of simulations will allow us to determine whether or not we can recover the full variation in rotation curve shapes that are seen in observations, which we will explore in a forthcoming study.

3.2 HI linewidths

The observations of V_{rot} relevant to this study are based on HI radio data, so we constructed mock HI data cubes. We derive HI line widths for the simulated galaxies, using inclinations 45° , 60°

and edge-on. In Fig 3 we show the global HI line profiles for inclinations of 60° , indicating 20% and 50% of the maximum flux by horizontal dashed and dot-dashed lines respectively. The quoted values of W_{50} and W_{20} in Table 1 are calculated by taking the average of the inclination corrected line-widths from the different inclinations 45° , 60° and edge-on. The results we present do not change significantly if any single inclination is chosen.

Fig 4 shows the ratio W_{50}/W_{20} as a function of $W_{20}/2$ for the simulations (red circles) and HIPASS data (Meyer et al. 2004 black dots). The relation $W_{20}=W_{50}+25$ is also shown (cyan line), the typical difference between the observed W_{20} and W_{50} (Koribalski et al. 2004; Bradford et al. 2015). The offset between W_{50} and W_{20} becomes significant for lower velocities/masses, with the relation $W_{50} \sim W_{20} - 25$ implying that at $W_{20}/2 = [50, 40, 30]$, $W_{50}/2$ is $[25, 31, 42]$ per cent lower. Our simulations suggest that this simple relation holds down to very low velocities/masses.

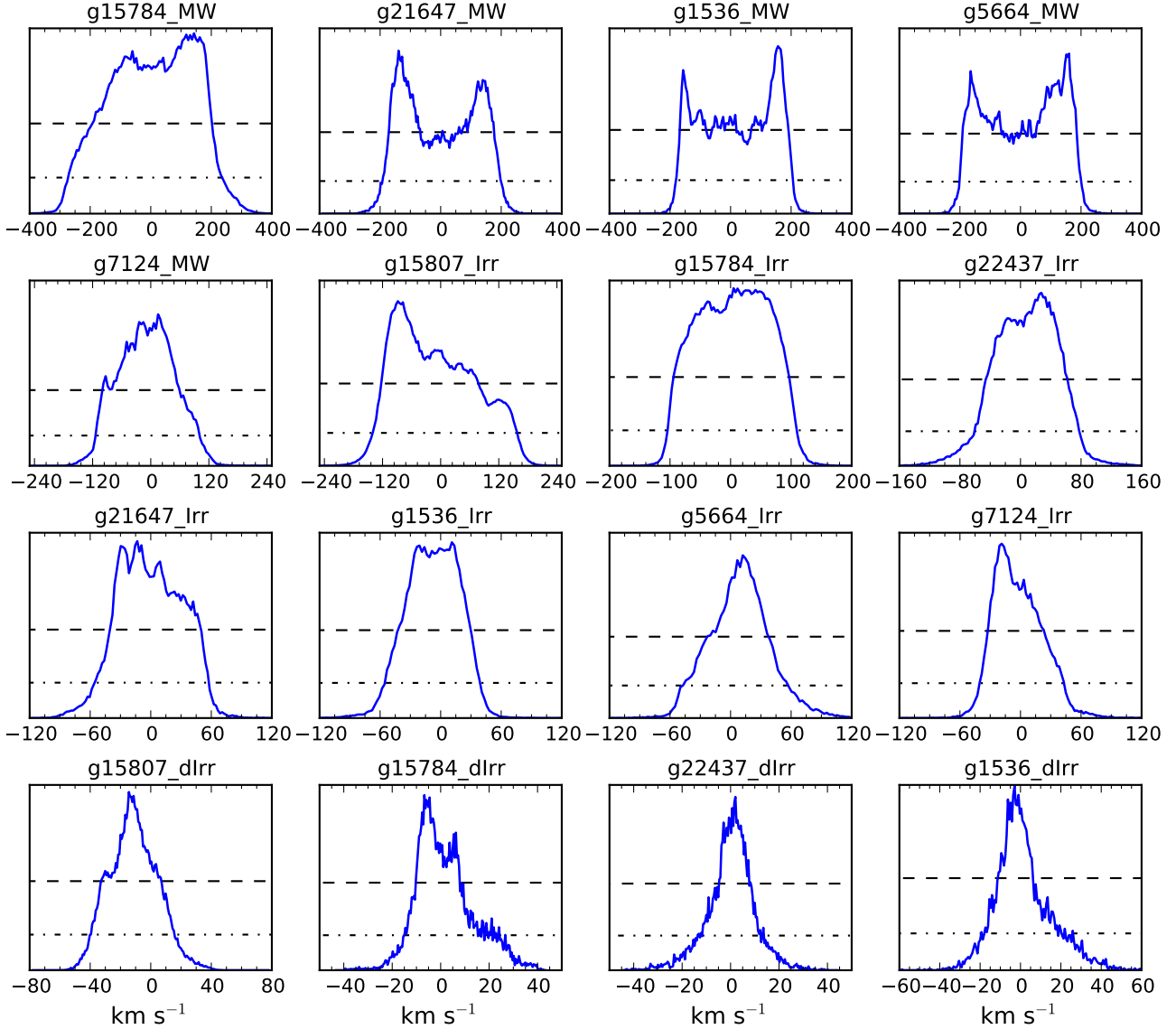


Figure 3. HI line profiles of the MaGICC galaxies, shown for inclinations of 60° in each case.

3.3 Measurements of rotation velocity

We note some nomenclature used in this paper:

- V_{flat} : the circular velocity at the flat part of the rotation curve.
- R_{flat} : the radius at which V_{flat} is reached.
- V_{last} : the circular velocity at the last point of the HI disc.
- R_{HI} : the extent of the HI disc: defines where V_{last} is measured.
- D_{HI} : diameter of the HI disc: $2 \times R_{\text{HI}}$.
- $V_{\text{max}}^{\text{DM}}$: the V_{max} from the DM only simulations.
- $R_{\text{max}}^{\text{DM}}$: the radius at which $V_{\text{max}}^{\text{DM}}$ is reached.
- h : disc scale length.

The criteria for selecting flat rotation curves in Stark et al. (2009) requires that V_{rot} measured at 3 disc scale lengths ($3h$) is 85 per cent of V_{last} , or in cases where R_{HI} is greater than $4h$, then V_{rot} measured at $4h$ is required to be 90 per cent of V_{last} . This definition has a degree of arbitrariness, as it depends on the relative distance between R_{HI} and integer multiples of h . In this study, we define rotation curves to be flat in the regions where V_{rot} changes by less

than 5 per cent between integer multiples of h . We define V_{flat} at the flattest of these flat regions, i.e. where the change in V_{rot} is the smallest, within the HI disc (in regions where $\text{radius} < R_{\text{HI}}$). V_{flat} is measured at the centre of the flattest region within the HI disc.

Our flatness criteria are better defined than those used in Stark et al. (2009), and are also stricter for galaxies with $R_{\text{HI}} < 5h$, (69 per cent of galaxies in the Swaters et al. 2009 data set from which Stark et al. 2009 was largely drawn), is at least as strict for galaxies with $5h < R_{\text{HI}} < 6h$ (a further 9 per cent of Swaters et al. 2009 galaxies), but may not be as strict for galaxies with $R_{\text{HI}} > 6h$ (12 per cent of Swaters et al. 2009 sample).

Some of our low mass simulated galaxies do not have any flat regions at radii lower than R_{HI} . These are deemed to be galaxies with slowly rising rotation curves. In such cases, marked with † in Table 1, we continue beyond R_{HI} until we find the first flat region of the rotation curve, i.e. a region where V_{rot} increases by less than 5 per cent as radius increases by h . V_{flat} is then measured at the central point of this flat region. Galaxies with rising rotation curves will be identified in our BTFR plot, and are analogous to those

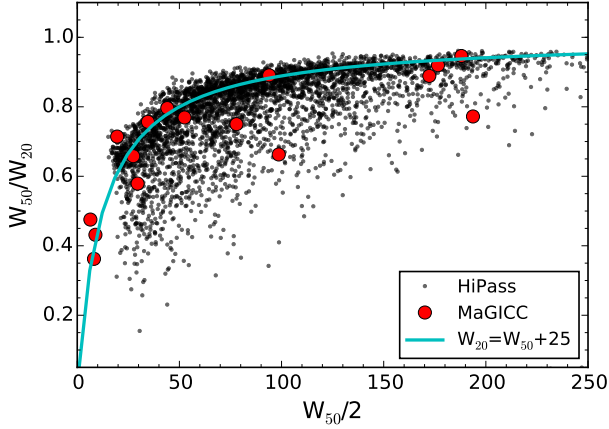


Figure 4. The ratio W_{50}/W_{20} plotted as a function of $W_{20}/2$ for the simulations (red circles) overlaid on HiPass data (black dots), with the relation $W_{20}=W_{50}+25$, also shown as a cyan line.

galaxies that are *excluded* in studies of observed V_{flat} BTFRs (e.g. Stark et al. 2009; McGaugh 2012; McGaugh & Schombert 2015).

3.4 The Baryonic Tully-Fisher relation

Figure 5 shows the different BTFRs for the different V_{rot} measurements of our simulated suite of galaxies. These are: V_{flat} (orange circles), V_{last} defined using $1 \text{ M}_{\odot}/\text{pc}^{-2}$ (purple squares) and 10^{19} cm^{-2} (green squares), V_{DHI} (blue stars) which uses the observed M_b - R_{last} relation to determine the radius to measure V_{rot} based on the M_b of each simulation, $W_{20}/2$ (pink triangles), $W_{50}/2$ (red diamonds) and $V_{\text{max}}^{\text{DM}}$ (black crosses).

Overplotted are observational BTFRs: the solid line shows the fit found in Lelli et al. (2016) using V_{flat} from observations of gas-rich galaxies $\log(M_b)=3.95\log(V_{\text{flat}})+1.86$, a relation very similar to that found in McGaugh & Schombert (2015); the dashed line shows the relation found by Bradford et al. 2015 using W_{20} measurements of galaxies selected from the Sloan Digital Sky Survey, $\log(W_{20}/2)=0.27\log(M_b)-0.672$; the dotted line shows the W_{50} relation determined by using $W_{50}=W_{20}-25$. We found a similar W_{50} BTFR using local volume data as compiled by Karachentsev et al. 2013, but do not overplot here as it adds to clutter without adding information. We also show a theoretical (dot-dashed) line from Di Cintio & Lelli (2016), which uses a semi-empirical model within a Λ Cold Dark Matter cosmology, measured in the flat region of the rotation curve.

For simulated galaxies with $M_b \gtrsim 2 \times 10^8 M_{\odot}$ the V_{flat} , V_{last} and W_{20} BTFRs are similar. This corresponds to galaxies with $V_{\text{rot}} \gtrsim 45 \text{ km s}^{-1}$ living in halos with $M_{\text{halo}} \gtrsim 5 \times 10^{10} M_{\odot}$. W_{20} and W_{50} are integrated measurements that are intrinsically more sensitive to contribution from the rising part of the rotation curves at small radii, which contains most of the HI flux, explaining their difference with V_{last} . The difference $W_{50} \sim W_{20} - 25$ holds over a large range of masses, meaning that the W_{50} BTFR does not have a large offset from the other measures of V_{rot} for massive galaxies: at $W_{20}/2=[100, 150, 200]$, $W_{50}/2$ is about $[12, 9, 6]$ per cent lower than the other measures of V_{rot} .

The V_{DHI} BTFR differs from V_{last} , indicative of the sensitivity of low mass galaxies to the radius at which V_{rot} is measured. This V_{DHI} BTFR also shows increased scatter at the the HI low

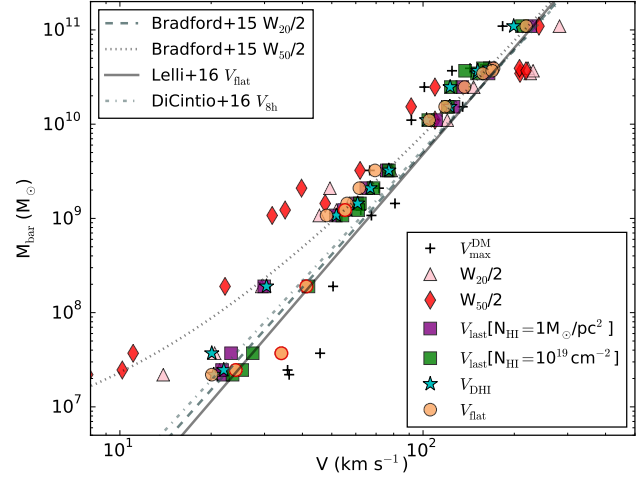


Figure 5. BTFRs for the MaGICC galaxies. Different symbols show the relations obtained when using different V_{rot} measures: V_{flat} (orange circles), V_{last} (green squares), V_{DHI} (blue stars), $W_{20}/2$ (pink triangles), $W_{50}/2$ (red diamonds) and $V_{\text{max}}^{\text{DM}}$ (black crosses). The solid line is the observational BTFR obtained from gas-rich galaxies using V_{flat} in McGaugh & Schombert (2015). The dashed line is the $W_{20}/2$ BTFR from Bradford et al. (2015), while the dotted line adjusts this $W_{20}/2$ relation using $W_{50}=W_{20}-25$, the typical difference between these values as found in Bradford et al. (2015). The V_{flat} of simulated galaxies with rising rotation curves at their outer point are indicated by a solid red outline: these would be excluded from observed V_{flat} BTFRs.

mass end, but this is a region where scatter in the observed BTFRs also increases (see e.g. McGaugh 2012; Lelli et al. 2014).

For galaxies with $M_b \lesssim 10^8 M_{\odot}$, the different forms of the BTFR increasingly diverge. The V_{last} using threshold of 10^{19} cm^{-2} BTFR of the simulations follow closely the V_{flat} value of McGaugh & Schombert (2015), which is also close to the V_{flat} BTFR from Stark et al. (2009).

The V_{flat} BTFR from the simulations also follows the observed V_{flat} BTFR if the galaxies with rising rotation curves are neglected, as they are in the observational derivations. Such galaxies are marked with red outlines in Fig 5. Our model suggests that low mass galaxies with rising rotation curves would fall off the V_{flat} BTFR, having excessively high values of V_{rot} , if their gas discs would extend far enough for V_{flat} to be measured.

We also show results from the corresponding dark matter only simulations, which shows how the measured V_{rot} of disc galaxies becomes a smaller fraction of $V_{\text{max}}^{\text{DM}}$. This is due to two related effects: primarily, R_{HI} becomes a smaller fraction of $R_{\text{max}}^{\text{DM}}$ for low mass galaxies, which are confined to the inner regions of DM halos (compare R_{HI} to $R_{\text{max}}^{\text{DM}}$ in Table 1, and see also Fig 7 of Brook & Shankar 2015); secondly, baryons are able to cool to the central regions of halos, so galaxies with high baryonic masses, i.e. high mass galaxies, have more steeply rising rotation curves in general, meaning that V_{rot} becomes close to $V_{\text{max}}^{\text{DM}}$ at relatively small radii.

The shape of dark matter halos can be affected by baryons by either adiabatic contraction (Blumenthal et al. 1986), or expansion (see Pontzen & Governato 2014, for a review). The competing processes mean that the final profile can depend on the amount of gas inflowing to the central region causing contraction, and the timescale and mass of gas outflows causing expansion. Simulations suggest that this results in dark matter density profile shapes being dependent on galaxy mass (Di Cintio et al. 2014b; Chan et al. 2015;

Table 2. Slopes (a) and zero points (b) of the various BTFRs

V_{rot}	a	b
$V_{\text{max}}^{\text{DM}}$	5.19	-.52
$W_{20/2}$	3.13	3.78
$W_{50/2}$	2.70	4.83
$V_{\text{last}}[\text{N}_{\text{HI}} = 1\text{M}_{\odot} \text{ pc}^{-2}]$	3.51	2.85
$V_{\text{last}}[\text{N}_{\text{HI}} = 10^{19} \text{ cm}^{-2}]$	4.02	1.85
V_{DHI}	3.56	2.80
V_{flat}	3.72	2.43

Tollet et al. 2016). The rotation curve shapes in the galaxies of this study have been affected by these processes, but as stated above, the detailed study of these shapes is beyond the scope of this paper.

Bearing in mind that a larger number of simulations may be required to define a low mass BTFR, we nevertheless show in Table ?? the best fits to the various BTFRs from Fig. 5, with the form $\log M_{\text{bar}} = a \log V_{\text{rot}} + b$. The difference in slopes between the various forms is significant. We do note that linear fits cannot always be appropriate, for example the relation $W_{20} = W_{50} + 25$ as shown in Fig. 4 implies that if the W_{20} BTFR is well fit by a linear relation, then W_{50} would not be.

4 DISCUSSION

We have made various measurements of V_{rot} for a suite of simulated galaxies within a Λ CDM context, and derived the corresponding BTFRs. Measuring V_{rot} using V_{flat} , V_{last} , V_{DHI} , W_{20} , W_{50} and $V_{\text{max}}^{\text{DM}}$ result in significantly different BTFRs, as the different measures of V_{rot} are found to diverge at low masses. Each BTFR derived using the different measures of V_{rot} from the simulations is consistent with the corresponding observed BTFRs in cases where observations are possible, i.e. V_{last} , V_{flat} , V_{DHI} , W_{20} , W_{50} .

Correspondence is found between simulations and observations in the V_{flat} case when appropriate selection of galaxies with flat rotation curves is made, excluding galaxies with rising rotation curves. The simulations indicate that galaxies with rising rotation curves would generally fall off the BTFR if their gas discs extended far enough to measure out to the flat part of the rotation curve.

We conclude that there is no single BTFR, with the relation between the baryonic mass and the rotation velocity of galaxies taking many forms which diverge significantly for low mass galaxies. Differences in the BTFR for different measures of V_{rot} have been shown for observed galaxies (Verheijen 2001; Noordermeer & Verheijen 2007; McGaugh 2012; Bradford et al. 2016). We show that the BTFR for simulated galaxies also depends on the manner in which rotation velocity is measured, with the BTFRs becoming increasingly different from one another for low mass galaxies.

The various forms of the BTFR emerge from the fundamental processes in galaxy formation, relating to fundamental forces, mass acquisition, angular momentum acquisition, baryon content, gas cooling, star formation, and energy feedback. BTFRs are thus crucial constraints on models that attempt to capture these fundamental processes of galaxy formation, not only in terms of understanding the relation between baryonic and total mass in galaxy populations, but also in terms of the velocity function (Brook & Shankar 2015), i.e. understanding the BTFR has important implications for how we compare the number of galaxies observed as a function of V_{rot} , to the number predicted in an Λ CDM cosmology.

Our hydrodynamical simulations of galaxy formation can explain the various forms of the BTFR within a Λ CDM context. It is instructive to compare our study with two recent Λ CDM cosmological models that have used the BTFR as a constraint, Trujillo-Gomez et al. (2011) and Dutton (2012).

In Trujillo-Gomez et al. (2011), a model population was made by matching M_* to M_{halo} following abundance matching, and giving each model galaxy an empirically motivated gas fraction and scale-length. A BTFR was derived by measuring circular velocities at 10 kpc. For galaxies at the high mass end of our study, correspondence with Trujillo-Gomez et al. (2011) is good. This is expected because R_{HI} extends far enough to reflect the value of V_{rot} at 10 kpc. For low mass galaxies, the Trujillo-Gomez et al. (2011) BTFR bends toward values of relatively high velocity, in a manner that is very similar to our $V_{\text{max}}^{\text{DM}}$ BTFR. This is also expected, because $R_{\text{max}}^{\text{DM}}$ is ~ 10 kpc for such galaxies, as seen in our Table 1, and such galaxies have very low baryon fractions meaning that DM only simulations are not greatly different from their model galaxies.

Dutton (2012) use a semi-analytic model population of galaxies, tuned to match the empirical M_* - M_{halo} and specific angular momentum- M_{halo} relations. They define V_{flat} as the circular velocity measured at the radius that contains 80 per cent of the cold gas. This is analogous to our V_{last} , so it is not surprising that both studies match the V_{flat} BTFRs from Stark et al. (2009). Dutton (2012) does not test whether all their model galaxies' rotation curves are actually flat; the rotation curves in some low mass galaxies may still be rising at the point they measure ' V_{flat} '. In fact, correspondence with observations *requires* the existence of low mass galaxies that have rising rotation curves, as was found in our simulations.

The rising rotation curves of many low mass galaxies means that one needs to take particular care when comparing models and theory. Measuring the V_{flat} BTFR for low mass galaxies requires a selection, with galaxies with rising rotation curves discarded. It is not clear whether this introduces a bias. For example, do low mass galaxies with extended HI discs and flat rotation curves fit on the average M_* - M_{halo} relation?

Measuring the V_{last} BTFR, on the other hand, is somewhat arbitrary, with the position of measurement determined by the radial extent of the cold gas. The large difference between R_{HI} and $R_{\text{max}}^{\text{DM}}$ highlights that V_{rot} may increase significantly in some cases, if HI discs extended further and allowed measurements at larger radii.

In fact, even when our low mass simulated galaxies meet the criteria for V_{flat} , i.e. they rise by less than five per cent when radius increases by h , they are still measured at a radius that can be a small fraction of $R_{\text{max}}^{\text{DM}}$. In these cases, even small gradients in the rotation curve can result in significant difference between the measured V_{flat} and the V_{rot} that would be reached if the cold gas extended far enough to measure rotation velocities at their peak value.

To proceed in confronting models with observations, it is suggested to test the BTFR as measured in different ways, at a variety of radii. This also facilitates the evaluation of the variation of rotation curve shapes, which provide further important constraints on galaxy formation models (Gentile et al. 2007; McGaugh et al. 2007; Oman et al. 2015; Brook 2015). Measuring at radii smaller than R_{flat} may also allow different cosmological models to be differentiated (Brook & Di Cintio 2015)

Even better is to exploit the important information provided by the entire rotation curve data of a large sample of galaxies. In a Λ CDM model, one can relate the halo mass as inferred from the fit to the rotation curve to M_b , and compare this relation to the M_b - M_{halo} relation that emerges from abundance matching studies. We will undertake such a procedure in a forthcoming study (Katz, H

et al. in prep), comparing a Λ CDM model that assumes an NFW profile (Navarro et al. 1996) with a model where DM halo shapes are modified by baryons (Di Cintio et al. 2014a).

ACKNOWLEDGEMENTS

We thank the anonymous referee for helpful suggestions. CB thanks MINECO (Spain) for financial support through the grant AYA2012-31101 and the Ramon y Cajal program. We thank DEISA for access to computing resources through DECI projects SIMU-LU and SIMUGAL-LU and the allocation of resources from STFC's DiRAC Facility (COSMOS: Galactic Archaeology), the DEISA consortium, co-funded through EU FP6 project RI-031513 and the FP7 project RI-222919 (through the DEISA Extreme Computing Initiative), the PRACE-2IP Project (FP7 RI-283493).

REFERENCES

- Abel T., Anninos P., Zhang Y., Norman M. L., 1997, *NewA*, 2, 181
- Begum A., Chengalur J. N., Karachentsev I. D., Sharina M. E., Kaisin S. S., 2008, *MNRAS*, 386, 1667
- Blumenthal G. R., Faber S. M., Flores R., Primack J. R., 1986, *ApJ*, 301, 27
- Bradford J. D., Geha M. C., Blanton M. R., 2015, *ApJ*, 809, 146
- Bradford J. D., Geha M. C., van den Bosch F. C., 2016, *ArXiv e-prints*
- Broeils A. H., Rhee M.-H., 1997, *A&A*, 324, 877
- Brook C., Shankar F., 2015, *ArXiv e-prints*
- Brook C. B., 2015, *MNRAS*, 454, 1719
- Brook C. B., Di Cintio A., 2015, *MNRAS*, 453, 2133
- Brook C. B., Stinson G., Gibson B. K., Wadsley J., Quinn T., 2012, *MNRAS*, 424, 1275
- Catinella B., Giovanelli R., Haynes M. P., 2006, *ApJ*, 640, 751
- Chan T. K., Kereš D., Oñorbe J., Hopkins P. F., Muratov A. L., Faucher-Giguère C.-A., Quataert E., 2015, *MNRAS*, 454, 2981
- Di Cintio A., Brook C. B., Dutton A. A., Macciò A. V., Stinson G. S., Knebe A., 2014a, *MNRAS*, 441, 2986
- Di Cintio A., Brook C. B., Macciò A. V., Stinson G. S., Knebe A., Dutton A. A., Wadsley J., 2014b, *MNRAS*, 437, 415
- Di Cintio A., Lelli F., 2016, *MNRAS*, 456, L127
- Dutton A. A., 2012, *MNRAS*, 424, 3123
- Dutton A. A., van den Bosch F. C., 2009, *MNRAS*, 396, 141
- Freeman K. C., 1999, in *Astronomical Society of the Pacific Conference Series*, Vol. 170, *The Low Surface Brightness Universe*, Davies J. I., Impey C., Phillips S., eds., p. 3
- Geha M., Blanton M. R., Masjedi M., West A. A., 2006, *ApJ*, 653, 240
- Gentile G., Tonini C., Salucci P., 2007, *A&A*, 467, 925
- Girardi L. et al., 2010, *ApJ*, 724, 1030
- Karachentsev I. D., Makarov D. I., Kaisina E. I., 2013, *AJ*, 145, 101
- Klypin A., Karachentsev I., Makarov D., Nasonova O., 2014, *ArXiv e-prints*
- Knollmann S. R., Knebe A., 2009, *ApJS*, 182, 608
- Koribalski B. S. et al., 2004, *AJ*, 128, 16
- Kuzio de Naray R., McGaugh S. S., de Blok W. J. G., Bosma A., 2006, *ApJS*, 165, 461
- Lelli F., Fraternali F., Verheijen M., 2013, *MNRAS*, 433, L30
- Lelli F., McGaugh S. S., Schombert J. M., 2016, *ApJ*, 816, L14
- Lelli F., Verheijen M., Fraternali F., 2014, *A&A*, 566, A71
- Marigo P., Girardi L., Bressan A., Groenewegen M. A. T., Silva L., Granato G. L., 2008, *A&A*, 482, 883
- McGaugh S. S., 2005, *ApJ*, 632, 859
- McGaugh S. S., 2012, *AJ*, 143, 40
- McGaugh S. S., de Blok W. J. G., Schombert J. M., Kuzio de Naray R., Kim J. H., 2007, *ApJ*, 659, 149
- McGaugh S. S., Schombert J. M., 2015, *ApJ*, 802, 18
- McGaugh S. S., Schombert J. M., Bothun G. D., de Blok W. J. G., 2000, *ApJ*, 533, L99
- Meyer M. J. et al., 2004, *MNRAS*, 350, 1195
- Navarro J. F., Frenk C. S., White S. D. M., 1996, *ApJ*, 462, 563
- Noordermeer E., van der Hulst J. M., Sancisi R., Swaters R. A., van Albada T. S., 2005, *A&A*, 442, 137
- Noordermeer E., Verheijen M. A. W., 2007, *MNRAS*, 381, 1463
- Obreschkow D., Croton D., De Lucia G., Khochfar S., Rawlings S., 2009, *ApJ*, 698, 1467
- Oh S.-H., de Blok W. J. G., Brinks E., Walter F., Kennicutt, Jr. R. C., 2011, *AJ*, 141, 193
- Oman K. A. et al., 2015, *MNRAS*, 452, 3650
- Papastergis E., Martin A. M., Giovanelli R., Haynes M. P., 2011, *ApJ*, 739, 38
- Pontzen A., Governato F., 2014, *Nature*, 506, 171
- Pontzen A., Roškar R., Stinson G. S., Woods R., Reed D. M., Coles J., Quinn T. R., 2013, *pynbody: Astrophysics Simulation Analysis for Python. Astrophysics Source Code Library*, ascl:1305.002
- Rahmati A., Pawlik A. H., Raičević M., Schaye J., 2013a, *MNRAS*, 430, 2427
- Rahmati A., Schaye J., Pawlik A. H., Raičević M., 2013b, *MNRAS*, 431, 2261
- Roberts M. S., Rots A. H., 1973, *A&A*, 26, 483
- Rubin V. C., Thonnard N., Ford, Jr. W. K., 1978, *ApJ*, 225, L107
- Santos-Santos I. M., Brook C. B., Stinson G., Di Cintio A., Wadsley J., Domínguez-Tenreiro R., Gottlöber S., Yepes G., 2016, *MNRAS*, 455, 476
- Schaye J. et al., 2015, *MNRAS*, 446, 521
- Shen S., Wadsley J., Stinson G., 2010, *MNRAS*, 407, 1581
- Sofue Y., Rubin V., 2001, *ARA&A*, 39, 137
- Sorce J. G., Guo Q., 2016, *MNRAS*
- Stark D. V., McGaugh S. S., Swaters R. A., 2009, *AJ*, 138, 392
- Stinson G., Seth A., Katz N., Wadsley J., Governato F., Quinn T., 2006, *MNRAS*, 373, 1074
- Stinson G. S., Bailin J., Couchman H., Wadsley J., Shen S., Nickerson S., Brook C., Quinn T., 2010, *MNRAS*, 408, 812
- Stinson G. S., Brook C., Macciò A. V., Wadsley J., Quinn T. R., Couchman H. M. P., 2013, *MNRAS*, 428, 129
- Swaters R. A., Sancisi R., van Albada T. S., van der Hulst J. M., 2009, *A&A*, 493, 871
- Swaters R. A., van Albada T. S., van der Hulst J. M., Sancisi R., 2002, *A&A*, 390, 829
- Tollet E. et al., 2016, *MNRAS*, 456, 3542
- Trujillo-Gomez S., Klypin A., Primack J., Romanowsky A. J., 2011, *ApJ*, 742, 16
- Verheijen M. A. W., 2001, *ApJ*, 563, 694
- Wadsley J. W., Stadel J., Quinn T., 2004, *NewA*, 9, 137
- Yegorova I. A., Salucci P., 2007, *MNRAS*, 377, 507
- Zavala J., Jing Y. P., Faltenbacher A., Yepes G., Hoffman Y., Gottlöber S., Catinella B., 2009, *ApJ*, 700, 1779